RSC Advances

ROYAL SOCIETY OF CHEMISTRY

www.rsc.org/advances

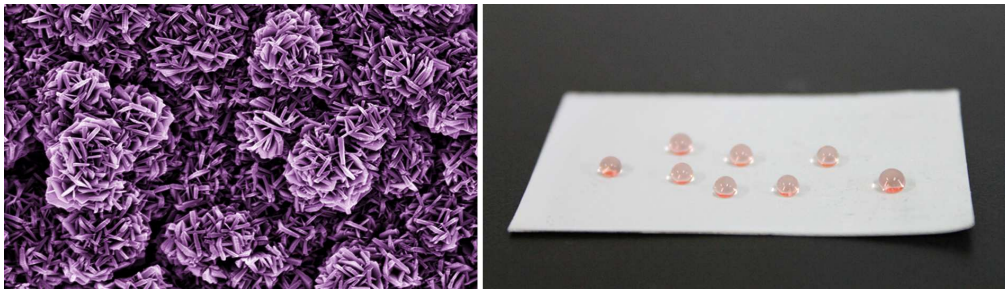

Super-hydrophobic lotus leaf like surface has been fabricated via growth of flower-like boehmite on 2024 aluminum alloy surface and subsequent POTS modification.

Cite this: DOI: 10.1039/c0xx00000x

www.rsc.org/xxxxxx

ARTICLE TYPE

In Situ Growth of Hierarchical Boehmite on 2024 Aluminum Alloy Surface as Superhydrophobic Materials

Zhijie Wang [a], Jinghua Gong [a], Jinghong Ma *[a], Jian Xu* [a,b]

Received (in XXX, XXX) Xth XXXXXXXXX 20XX, Accepted Xth XXXXXXXXX 20XX

DOI: 10.1039/b000000x

A super-hydrophobic 2024 aluminum alloy surface with multi-scale hierarchical flower-like boehmite (γ-AlOOH) structure has been fabricated via a facile hydrothermal approach. The differerent morphologies of the γ-AlOOH films were totally controlled by the preparation conditions for crystal growth, such as reaction solution and time. The morphology and structure of the films were characterized using scanning electron microscope (SEM), Fourier-transform infrared (FTIR), X-ray diffraction(XRD), and transmission electron microscopy(TEM). The super-hydrophobicity can be attributed to both the rough multi-scale structural boehmite coating and surface enrichment of low surface energy with the chemical vapor deposition of 1*H*,1*H*,2*H*,2*H*-Perfluorodecyltriethoxysilane (POTS). The resulting super-hydrophobic surface exhibits a water contact angle of 155° and a sliding angle of about 5°. The corrosion behavior was investigated with potentiodynamic polarization measurements and it was found that the super-hydrophobic coating considerably improved the corrosion resistant performance of aluminum alloy.

Introduction

Super-hydrophobic surfaces have generated significant attention due to their superior physico-chemical properties and important potential applications in many fields,[1-9] such as self-cleaning,[10-12] anti-corrosion,[13] oil/water separation,[14-16] anti-reflection,[17, 18] iridescence,[19, 20] anti-bioadhesion,[21, 22] and microdroplet transportation.[23] Superhydrophobicity exists inherently on the surfaces of many natural tissues, plants, and animal bodies. The most classic example is the lotus leaf surface, which has inspired researchers around the world because of its self-cleaning and water-repellent properties. Wettability is governed by both the surface chemical composition and geometric structure. Therefore, the strategy of creating a rough structure on an intrinsically hydrophobic surface or chemically modifying a rough surface with low surface free energy compounds is usually used to fabricate superhydrophobic surfaces.

Aluminum alloy is essential for research because it is abundant in nature, easy to handle and it is an important material due to its wide range of industrial applications,[24-27] especially in aerospace and household industries. Special 2024 aluminum alloy with high intensity and toughness is applied as building materials including antenna, door and window jamb, roof and building enclose, etc. However, a major disadvantage of aluminum alloy is that it corrodes easily in humid environments,[26, 28] which limits its practical application. The fabrication of super-hydrophobic surfaces for aluminum alloy is one of the novel methods to protect against corrosion. The research on super-hydrophobic surfaces has made considerable progress in recent years, and various fabrication methods have been reported the preparation of super-hydrophobic aluminum alloy surfaces through the combination of chemical composition and surface multi-scale structures, especially flowerlike boehmite thin film [18, 29-32]. Among them, chemical etching [9, 33-35] and surface coating [29, 36-39] are usually employed to introduce a multi-scale scale roughness on the aluminum alloy substrate. However, the coating method always involves complicated process as it needs to prepare coating precursor first. Meanwhile, the coating materials usually have poor adhesive force against their substrates. And the chemical etching can lead to a permanent damage of aluminum substrate. Therefore, it is highly desirable to develop a facile method for the fabrication of stable superhydrophobic aluminum surfaces.

In our previous works, we recently showed that γ-AlOOH nanosheets film can be formed directly on AlOOH nanoparticle seed layer.[40] The thin film exhibits good adhesion and mechanical stability. In the subsequent experiments, we also found that the formation of the nanosheet films with special nanostructures could be tuned by changing the reaction time, reactant concentrations and temperature. Here, we designed and synthesized γ-AlOOH nanosheets thin films in situ growth on aluminum alloy substrate by a facile hydrothermal approach. Various morphology of γ-AlOOH 3D intricate flower-like patterns and 2D nanosheets structures can be selectively obtained by simply changing the type of reactants. Treatment with POTS, the resulting γ-AlOOH films with hierarchical micro/nanostructured show superhydrophobicity with water contact angles (CA) greater than 155°. Superhydrophobic film which provides a very effective corrosion-resistant coating for the underlying aluminum.

Experimental

Materials

Sodium aluminate ($NaAlO_2$) and urea (NH_2CONH_2) were purchased from Sinopharm Chemical Reagent; 1*H*,1*H*,2*H*,2*H*-Perfluorodecyltriethoxysilane (POTS 97%) was obtained from Sigma-Aldrich. All the reagents were used as received. The 2024 aluminum alloy plates were purchased from Shanghai E&I Light Alloy Group Co., Ltd. The chemical composition of 2024 aluminum alloy includes 93.5 wt% aluminum, 4.4 wt% copper, 1.5 wt% magnesium, and 0.6 wt% manganese.

Film fabrication process

In a typical experiment, 10.2 g of sodium aluminate ($NaAlO_2$) and 28.8 g of urea (NH_2CONH_2) were dissolved in 1 L of deionized water under stirring. 30 mL solution was transferred into a 50 mL Teflon-lined stainless steel autoclave, and a clean 2024 aluminum alloy slide was then immersed in the solution. The autoclave was sealed and heated in the oven at 160 °C for 2 h. After cooling to room temperature, the sample was rinsed with deionized water several times and finally dried in a vacuum oven at 50 °C for 6 h. Additional experiments, as those above, but with changes of reaction time from 10 min to 2 h, deionized water or urea deionized water mix solution as reaction solution, were carried out too.

And the as-treated samples were placed in a sealed vessel with POTS on the bottom for further chemical modification. The vessel was put in an oven at 120 °C for 2.5 h to enable the vapor of POTS to react with the OH groups on the slide surface. Finally, the slide was taken out of the vessel and placed in an oven of 150 °C for another 1.5 h to volatilize the unreacted POTS molecules on the surface.

Characterization

The contact angles (CAs) were measured on a contact angle instrument (Contact Angle SystemOCA40, Dataphysics Co., Germany) at room temperature. Measurements from at least six droplets of 5 μl of freshly distilled pure water were averaged. Attenuated total reflection Fourier transform infrared spectra (ATR-FTIR) was recorded using a Nicolet-8700 spectrometer equipped with ATR accessory. XRD spectroscopy was carried out on a Rigaku D/max 2550 V X-ray diffractometer using Cu-Kα irradiation (λ = 1.5406 Å). The operating voltage and current were kept at 40 kV and 300 mA, respectively. The morphology was observed using a transmission electron microscope (TEM，JEM-2100F) and a field-emission scanning electron microscope (FESEM, S-8010, Hitachi, Tokyo, Japan). The element composition was characterized by Oxford Instruments Inca X-Max energy dispersive X-ray (EDX) spectrometer associated with the FESEM instrument. Potentiodynamic polarization curves were obtained on an Autolab (PGSTAT302N potentiostat) using a standard three-electrode system in 100 ml of 3.5% (wt.%) NaCl solution (open to air) at room temperature. Sample with size of 1 cm^2 was used as the working elecrode during polarization tests. Saturated calomel was used as reference electrode (SCE) and a platinum sheet as counter electrode. The potentiodynamic measurements were taken between −800 and -200 mV versus SCE at a rate of 1 mV/s.

Reults and discussion

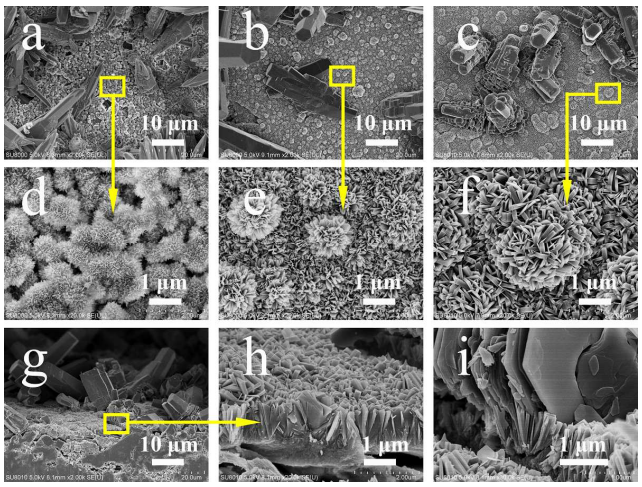

Fig.1 FE-SEM images of sample surfaces after hydrothermal treatment in sodium aluminate and urea mixed solution at 160 °C for different reaction time: (a) 10 min, (b) 30 min, and (c) 120 min. (d), (e), and (f) are the enlarged FE-SEM images of the indicated areas in (a), (b), and (c), respectively. (g), (h), and (i) are the cross section FE-SEM images of the sample prepared at 160 °C for 120 min.

The morphologies of the as-prepared films were characterized by field-emission scanning electron microscopy (FE-SEM). Fig. 1a-f show FE-SEM images of the sample surfaces after hydrothermal treatment at 160 °C for 10 min, 30 min, and 120 min, respectively. Some large irregular byproducts with varying shape were covered on the resulting 2024 aluminum alloy surface (Fig. 1a-c). Fig. 1d-f are the enlarged versions of the FE-SEM images shown in Fig. 1a-c, respectively. All the samples exhibit flower-like structures that are dispersed randomly on the surfaces.When the treatment time was only 10 min, the flower-like γ-AlOOH structures with diameters about 1 μm were randomly formed on the surfaces. Each of the flowers was composed of dozens of tiny and thin nanosheets. When treatment time increasing to 30 min, the flower-like γ-AlOOH structures covered on the surface were growing into bigger ones with diameters about 2 μm. The nanosheets became thicker and denser as the treatment time increased. In contrast, after treatment for over 120 min, these γ-AlOOH microcrystals have a platelike/sheet morphology and some of them assembled into large size flower-like structures with diameters about 3 μm. Each of the flowers was composed of dozens of nanosheets with thickness ranging from 50 to 100 nm (Fig. 1f). A cross-sectional view of the γ-AlOOH film (Fig. 1g-h) clearly demonstrates that the γ-AlOOH naonsheets film with a thickness of about 1.1 μm were assembled on the 2024 aluminum alloy substrate. The nanosheets were observed to be vertically aligned over the entire substrate surface and appeared to be partly in the form of multi-layers. Fig. 1i shows some of the byproducts are also composed of nanosheets and connected together perfectly with γ-AlOOH nanosheets. The formation of these irregular byproducts would be due to the random assembly of γ-AlOOH in the solution.

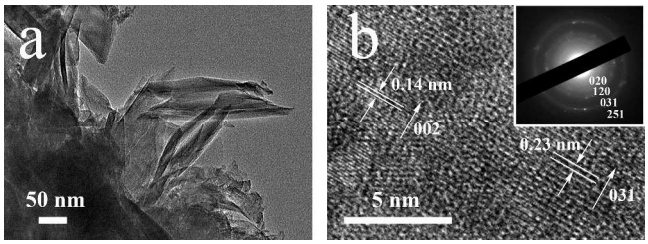

Fig. 2 (a) TEM image of nanosheets for a sample hydrothermally treated at 160 °C for 2 h; (b) HRTEM image of the nanosheet and ED pattern of the nanosheet in the insert image.

Fig. 2 shows the representative TEM images of the sample hydrothermally treated at 160 °C for 2 h, which further proves the same microstructural information as the SEM observations. As shown in Fig. 2a, the film was made up of flaky γ-AlOOH, several nanosheets with a thickness of 40 nm can be observed. In the HRTEM image (Fig. 2b) taken from the edge of the individual microstructure, (031) and (002) planes were marked, with the spacing of the adjacent lattice planes of 0.23 nm and 0.14 nm, which are very close to the theoretical values. The selected area electron diffraction (SAED) patterns exhibit rings corresponding to the [020], [120],[031] and [251] planes of γ-AlOOH. These patterns are consistent with the XRD patterns.

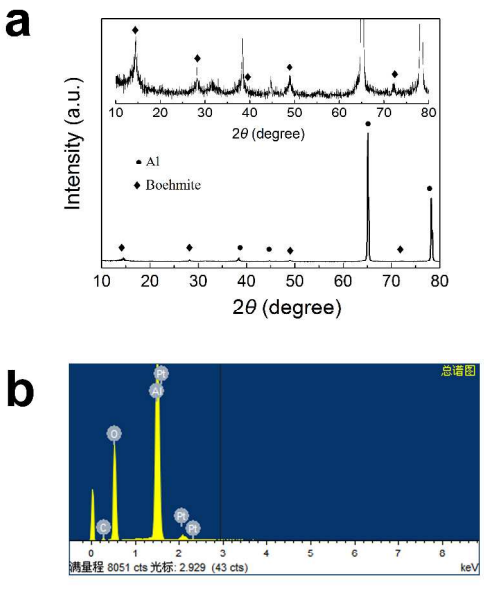

Fig.3 (a) XRD patterns and (b) EDX spectrum of the resultant boehmite film on the 2024 aluminum alloy prepared via the typical synthetic procedure at 160 °C for 2 h. Insets (a) shows the enlarged XRD pattern.

The XRD patterns of the 2024 aluminum alloy sample after hydrothermal treatment are shown in Fig. 3a. Four sharp and intensive diffraction peaks are assigned to the face-centered cubic (fcc) structure of metallic aluminum (JCPDS file no. 04-0787). The other diffraction peaks can be indexed according to the typical of orthorhombic boehmite phase (γ-AlOOH, JCPDS file No. 21-1307). Such weak and broad diffraction peaks indicate that the boehmite has a small crystalline size. The results confirm that the film growing out of the aluminum alloy surface is boehmite phase. EDX quantitative results shown in Fig. 3b indicate the presence of elements Al and O in the sample, in addition to the Pt peak originating from the Pt for increasing the conductivity of the SEM samples. The Al and O mainly come from γ-AlOOH. The Al/O atomic ratio is about 1.9, which is close to the theoretical value of 2 considering the instrumental error.

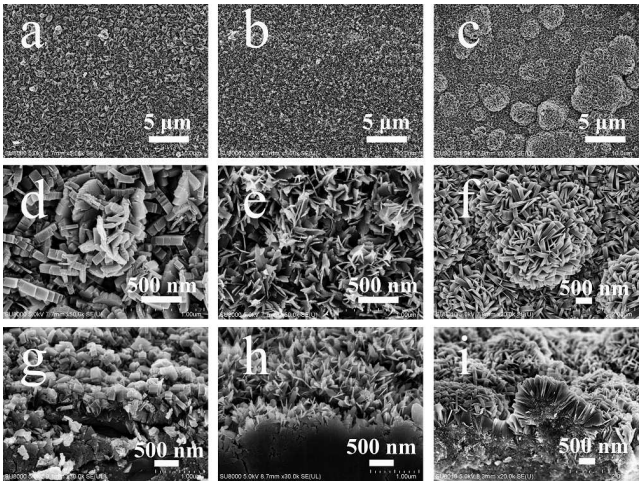

Fig.4 FE-SEM images of sample surfaces after hydrothermal treatment in water (a), urea solution (b), and sodium aluminate and urea mixed solution (c) at 160 °C for 2h; (d), (e) and (f) are the enlarged images of (a), (b), and (c), respectively; (g), (h) and (i) show the cross sections FE-SEM images of the samples corresponding to (a), (b) and (c), respectively.

We also conducted different hydrothermal solutions to compare, such as aqueous solution or urea solution, and all the processing with the same temperature. Fig. 4 shows FE-SEM images of sample surfaces after hydrothermal treatment in deionized water, urea solution, sodium aluminate and urea mixed solution at temperature of 160 °C for 2 h, respectively. In deionized water, we can clearly see the sample surface was composed of many zigzag like interlaced plates (Fig. 4d). When in the urea solution, the size and thickness of the nanosheets are smaller than those of the nanosheets prepared in deionized water (Fig. 4e). However, in the sodium aluminate and urea mixed solution, a more compact and larger size nanosheets were obtained, as shown in Fig. 4f and the nanosheets were assembled into papillae like structures. The cross sectional FE-SEM images indicate that all nanosheets were predominantly perpendicular to the substrate (Fig. 4g-h). And the sample growed in sodium aluminate and urea mixed solution with the highest thickness about 1 μm. Adding sodium aluminate was found to result in enlarged the thickness of film due to the extra supply of aluminum source for growth of γ-AlOOH. The control of the fine microstructures was achieved by varying hydrothermal solution.

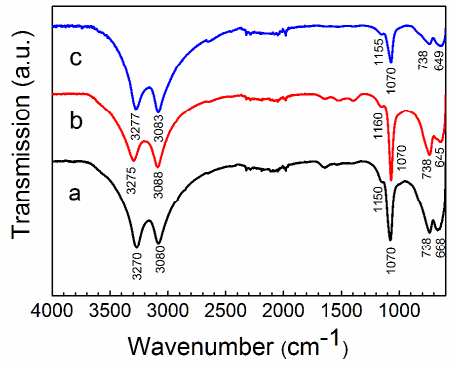

Fig. 5 FT-IR spectra of sample surfaces after hydrothermal treatment in water (a), urea solution (b), and sodium aluminate and urea mixed solution (c) at 160 °C for 2h.

Fig. 5 shows the FT-IR spectra of the samples hydrothermally treated at 160 °C for 2h in the region of 600-4000 cm^{-1}. The most predominant spectral feature is the intense sharp peak observed at 3277 and 3083 cm^{-1}, which can be assigned to the υ_{as} (Al)-OH and υ_s (Al)O-H stretching vibrations. Another sharp peak at 1070 cm^{-1} and the weak shoulder around 1155 cm^{-1} are respectively assigned to the δ_s Al-O-H and δ_{as} Al-O-H bending vibrations of the boehmite. The torsional mode of Al-O at 738 cm^{-1} and 649 cm^{-1} are also observed in the spectra. The FTIR analysis further confirms that the boehmite phase exists on the 2024 aluminum alloy surface. Moreover, these characteristic bands could be observed for all samples prepared in different solutions, which indicated that the formed nanoflakes have the same structure of γ-AlOOH.

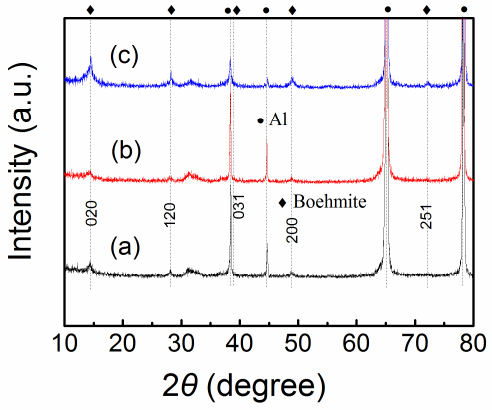

Fig.6 XRD patterns of sample surfaces after hydrothermal treatment in water (a), urea solution (b), and sodium aluminate and urea mixed solution (c) at 160 °C for 2h.

Fig. 6 shows the XRD patterns of the obtained samples after their hydrothermal treatment in deionized water, urea solution, and sodium aluminate and urea mixed solution at 160 °C for 2 h. In the case of all samples, some peaks attributable to the γ-AlOOH were clearly observed. The diffraction peaks are indexed according to the orthorhombic boehmite phase. This result is in agreement with the FT-IR spectra. A diffraction peak of [020] reflection, which has the highest intensity according to the JCPDS file number 21-1307 of γ-AlOOH. Under the urea solution the intensity of the diffraction peak corresponding to the [020] plane is lowest than other samples, and the peak were highest in sodium aluminate and urea mixed solution. This indicates that the content of the γ-AlOOH was lowest in urea solution, and highest in sodium aluminate and urea mixed solution. This result is in agreement with the SEM observations.

The control of the fine microstructures formed on 2024 aluminum alloy substrate was achieved by varying hydrothermal solution. The involved reactions for the formation of γ-AlOOH are suggested as follows:

$$Al + O_2 \rightarrow Al^{3+} \quad (1)$$

$$H_2O \rightarrow H^+ + OH^- \quad (2)$$

$$Al^{3+} + 3OH^- \rightarrow Al(OH)_3 \quad (3)$$

$$H_2N\text{-}CO\text{-}NH_2 + 3H_2O \rightarrow 2NH_4^+ + CO_2 + 2OH^- \quad (4)$$

$$AlO_2^- + 2H_2O \rightarrow Al(OH)_3 + OH^- \quad (5)$$

$$Al(OH)_3 \rightarrow \gamma\text{-}AlOOH + H_2O \quad (6)$$

In deionized water, the surface of alumimum alloy was eroded by OH^- produced by the hydrolysis of of H_2O to form $Al(OH)_3$ nuclei, and turned to γ-AlOOH nanosheets on the surface of alumnum alloy under a hydrothermal treatment at 160 °C. In the urea solution, the hydrolysis of urea gradually turned the solution weakly alkaline as the concentration of hydroxyl ions (OH^-) increased, and more $Al(OH)_3$ nucleis were formed. With the same grow rate the γ-AlOOH nanosheets were thinner than those formed in water. Since there was no other Al^{3+} in solution of water or urea solution, only 2D nanosheet arrays were formed on the aluminum alloy surface. The uniform "papillae" grown from 2D nanosheet arrays can not be found.

As to the sodium aluminate and urea mixed solution, not only the surface of the aluminum alloy formed the $Al(OH)_3$ nucleis and the AlO_2^- also turned into $Al(OH)_3$ nucleis in the solution. When the temperature was increased up to 160 °C, the preferentially nucleates on the aluminum alloy substrate were firstly turned into γ-AlOOH in a much shorter period of time, as the heterogeneous nucleation has a lower barrier energy than homogeneous nucleation in the solution. Then, the homogeneous $Al(OH)_3$ nucleates were turned into numerous γ-AlOOH nanoplatelets in the solution. Since the boehmite nanoplatelets have numerous surface-located hydroxyl groups, some of the γ-AlOOH nanosheets aggregated randomly. As the reaction proceeds, these two types of nuclei on substrate can result in nanostructures with different densities and morphologies on substrate. Thus, the γ-AlOOH nanosheets were assembled into hierarchical structures with multi-scale scale roughness.

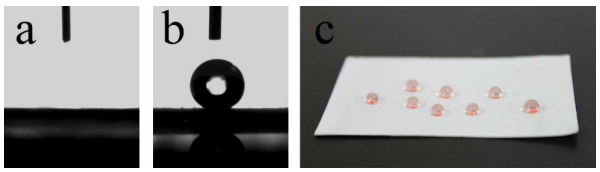

Fig. 7 (a) Shape of a water droplet on the surface of the as-prepared γ-AlOOH film on 2024 aluminum alloy obtained at 160 ℃ for 2 h. (b) Shape of a water droplet on the surface of the same film as in (a) after POTS hydrophobization; (c) image of the water on the film used in (a) after PFOT hydrophobization.

The wettability of the resultant surfaces was characterized in detail with water static CA measurements. When a water droplet was dripped on the as-prepared γ-AlOOH films, it spread onto the

surface very quickly, indicating the excellent superhydrophilic properties of this film (Fig.7a). Such a small CA is attributed to the presence of many -OH groups on the surface of the γ-AlOOH crystals, leading to superhydrophilicity. However, the surface of the sample became superhydrophobic after modification with POTS. The resultant surface was so hydrophobic that the water droplet deposited on the surface formed almost perfect sphere with a water CA of 155° (Fig. 7b), clearly revealing that the surface change from superhydrophilic to superhydrophobic. The sliding angle is about 5°, implying that the water droplets can be easily moved out of the surface. The optical image of water droplets with uniform size on the surface of the modified 2024 aluminum alloy surface (Fig. 7c) gives a direct demonstration of the superhydrophobicity of the treated film.

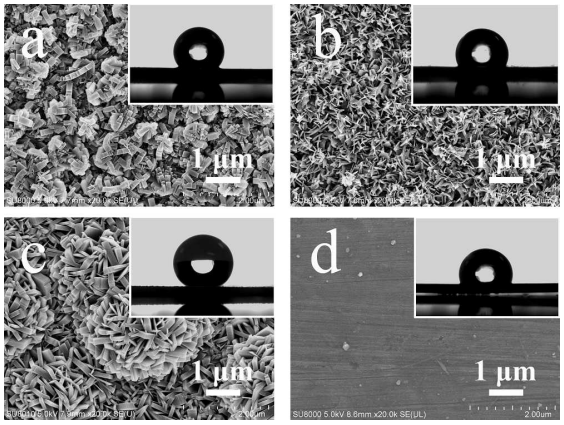

Fig. 8 FE-SEM images of sample surfaces after hydrothermal treatment in water (a), urea solution (b), sodium aluminate and urea solution (c) at 160 °C for 2h, and without any treated (d); the photographs of the 5 μL water droplet on different morphology samples surfaces after POTS modification

After modification with POTS, such different surfaces show very different water CA (insets of Fig.8). The wetting properties were evaluated by water CA measurements and the film sample obtained after hydrophobization treatment.Theories of wetting behaviors on the surfaces including Wenzel's model[41] and Cassie-Baxter's model[42] have been developed for single or dual micro/nano roughness scales. Wenzel's model describes the wettability of the surface which has been totally wet by liquid, and there is no trapped air between the liquid and the solid surface. The apparent CA θ_W is given as a function of r and θ:

$$\cos\theta_W = r\cos\theta \qquad (1)$$

where r is the dimensionless roughness and θ is the static CA on the smooth surfaces.

Cassie and Baxter model describes the wetting of a surface in which trapped air resides between the liquid and the solid, and the surface is not totally wet. Equation (2) describes the relationship between the CA of a water droplet on a smooth surface (θ) and the CA on a heterogeneous surface (θ_{CB}) composed of a solid and air.

$$\cos\theta_{CB} = f_1\cos\theta - f_2 \qquad (2)$$

Here, f_1 and f_2 are the fractions of solid surface and air in contact with liquid, respectively, that is, $f_1+f_2=1$. The water droplet maintains the hydrophobic Cassie-Baxter state on the hierarchical surfaces composed of different nanoscale roughnesses as shown in Fig. 8. The water contact angles of nanoscale flakes structures with different size were measured to be 132° (Fig. 8a) and 121° (Fig. 8b), respectively. In comparison, a flat aluminum alloy was also modified with POTS through the same chemical route. The CA of the modified smooth aluminum alloy surface was determined to be only 110° (Fig. 8d). On the basis of our experimental data, the f_2 values of the rough surfaces with nanosheets structures with different size are calculated to be 49.8% and 26.5%, respectively. The CA of the small size nanosheets is decreased due to the decrease of air trapped surface with smaller size nanoscale flakes. The CA of rough surface with 3D flowerlike structures was measured to be 155° (Fig. 8c) , the f_2 value was calculated to be 85.8%. The aboved results indicate that the achievement of superhydrophobicity is mainly a result of the large fraction of air trapped in the rough surface by combining 3D microstructures of flowerlike spheres with nanostructures of protuberances and cavities. On the other hand, it should be mentioned that the rough surfaces without modification by POTS are hydrophilic. This suggests that only a suitable multi-scale structure is not enough to obtain a superhydrophobic surface. By fine-tuning the size of hierarchical structure and modifying the as-prepared rough surface with different low-surface-energy coatings, it is possible for us to fabricate the superhydrophobic surface.

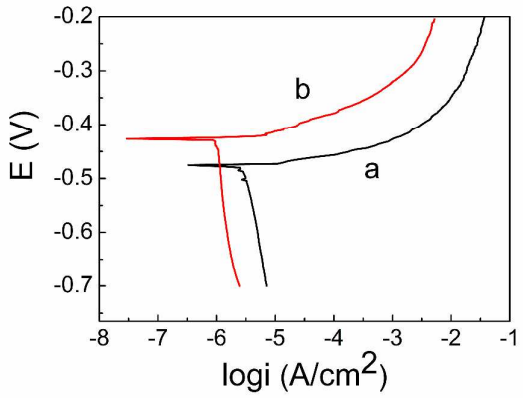

Fig. 9 Polarization curves (vs SCE) of samples immersed in 3.5□% aqueous sodium chloride solution at room temperature: (a) untreated bare aluminum alloy substrate, (b) superhydrophobic aluminum alloy substrate.

The corrosion behaviors of the superhydrophobic aluminum alloy surface and the untreated bare aluminum alloy surface were investigated via polarization curves in 3.5 wt.% NaCl solution. In a typical polarization curve, the positive shift of the Ecorr and the lower corrosion current densities correspond to lower corrosion rates and better corrosion resistance. The corrosion potential (Ecorr) positively increases from -0.475 V for the bare 2024 aluminum alloy (Fig. 9a) to -0.427 V for the superhydrophobic surface (Fig. 9b). The corrosion current density of the superhydrophobic film was smaller than that of the aluminum alloy substrate, which means that the superhydrophobic film is very effective in protecting the aluminum alloy from corrosion. It is generally believed that the air trapped in multi-scale cavities behaves as a dielectric for a parallel plate capacitor. Such an air dielectric can inhibit the electron transfer between the aluminum alloy substrate and the electrolyte, which strongly protects the underlying aluminum alloy substrate[43, 44].

Conclusions

In summary, we have demonstrated a facile method for tuning wetting properties by preparing nanosheets γ-AlOOH films with flower-like microstructures on a 2024 aluminum alloy substrate in a closed hydrothermal system. The resultant γ-AlOOH films were composed of complex papillae which are assembled from several nanosheets, exhibiting a multi-scale roughness. In particular, the thin films with different microstructures can be tailored by controlling the reaction solution and time. After simple hydrophobic treatment with POTS, such different morphology surfaces show very different water CA. Moreover, the 3D microstructures γ-AlOOH films show excellent superhydrophobicity with a CA of 155°. Such superhydrophobic surfaces also exhibit relatively good mechanical robustness and anticorrosion properties, which are favorable for the potential applications in various industrial items.

Acknowledgements

This research was supported by Shanghai Leading Academic Discipline Project (Project No: B603), Programme of Introducing Talents of Discipline to Universities (No. 111-2-04).

Notes and references

[a] *State Key Laboratory for Modification of Chemical Fibers and Polymer Materials, College of Material Science and Engineering, Donghua University, Shanghai 201620, P. R. China. E-mail: mjh68@dhu.edu.cn; Fax: +86-021-67792833 Tel: +86-021-67792833.*

[b] *Laboratory of Polymer Physics and Chemistry, Institute of Chinese Academy of Sciences, Beijing 100190, P. R. China. E-mail: jxu@iccas.ac.cn; Fax: +86-10-62657919; Tel: +86-10-62657919.*

† Electronic Supplementary Information (ESI) available: [details of any supplementary information available should be included here]. See DOI: 10.1039/b000000x/

‡ Footnotes should appear here. These might include comments relevant to but not central to the matter under discussion, limited experimental and spectral data, and crystallographic data.

1. X. Zhang, L. Wang and E. Levanen, *RSC Advances*, 2013, **3**, 12003-12020.
2. Y. L. Zhang, H. Xia, E. Kim and H. B. Sun, *Soft Matter*, 2012, **8**, 11217-11231.
3. X. Yao, Y. Song and L. Jiang, *Advanced Materials*, 2011, **23**, 719-734.
4. Z. Cheng, H. Lai, M. Du, S. Zhu, N. Zhang and K. Sun, *Soft Matter*, 2012, **8**, 9635-9641.
5. X. Wu, L. Zheng and D. Wu, *Langmuir*, 2005, **21**, 2665-2667.
6. F. Shi, X. Chen, L. Wang, J. Niu, J. Yu, Z. Wang and X. Zhang, *Chemistry of Materials*, 2005, **17**, 6177-6180.
7. L. Feng, S. Li, H. Li, J. Zhai, Y. Song, L. Jiang and D. Zhu, *Angewandte Chemie International Edition*, 2002, **41**, 1221-1223.
8. L. Feng, S. Li, Y. Li, H. Li, L. Zhang, J. Zhai, Y. Song, B. Liu, L. Jiang and D. Zhu, *Advanced Materials*, 2002, **14**, 1857-1860.
9. Z. Guo, F. Zhou, J. Hao and W. Liu, *Journal of the American Chemical Society*, 2005, **127**, 15670-15671.
10. W. Barthlott and C. Neinhuis, *Planta*, 1997, **202**, 1-8.
11. V. A. Ganesh, H. K. Raut, A. S. Nair and S. Ramakrishna, *Journal of Materials Chemistry*, 2011, **21**, 16304-16322.
12. X. Zhang, X. Liu, J. Laakso, E. Levanen and T. Mantyla, *Applied Surface Science*, 2012, **258**, 3102-3108.
13. Y. Zhu, J. Zhang, Y. Zheng, Z. Huang, L. Feng and L. Jiang, *Advanced Functional Materials*, 2006, **16**, 568-574.
14. J. Wu, N. Wang, L. Wang, H. Dong, Y. Zhao and L. Jiang, *ACS Applied Materials & Interfaces*, 2012, **4**, 3207-3212.
15. F. Zhang, W. B. Zhang, Z. Shi, D. Wang, J. Jin and L. Jiang, *Advanced Materials*, 2013, **25**, 4192-4198.
16. M. Jin, J. Wang, X. Yao, M. Liao, Y. Zhao and L. Jiang, *Advanced Materials*, 2011, **23**, 2861-2864.
17. W. L. Min, B. Jiang and P. Jiang, *Advanced Materials*, 2008, **20**, 3914-3918.
18. E. Yu, H. J. Lee, T. J. Ko, S. J. Kim, K. R. Lee, K. H. Oh and M. W. Moon, *Nanoscale*, 2013, **5**, 10014-10021.
19. J. N. Wang, R. Q. Shao, Y. L. Zhang, L. Guo, H. B. Jiang, D. X. Lu and H. B. Sun, *Chemistry – An Asian Journal*, 2012, **7**, 301-304.
20. D. Wu, Q. D. Chen, H. Xia, J. Jiao, B. B. Xu, X. F. Lin, Y. Xu and H. B. Sun, *Soft Matter*, 2010, **6**, 263-267.
21. R. Sheparovych, M. Motornov and S. Minko, *Advanced Materials*, 2009, **21**, 1840-1844.
22. T. Sun, H. Tan, D. Han, Q. Fu and L. Jiang, *Small*, 2005, **1**, 959-963.
23. X. Hong, X. Gao and L. Jiang, *Journal of the American Chemical Society*, 2007, **129**, 1478-1479.
24. B. Yin, L. Fang, J. Hu, A. Q. Tang, J. He and J. H. Mao, *Surface and Interface Analysis*, 2012, **44**, 439-444.
25. A. M. Abdel-Gaber, B. A. Abd-El-Nabey, I. M. Sidahmed, A. M. El-Zayady and M. Saadawy, *Materials Chemistry and Physics*, 2006, **98**, 291-297.
26. Y. Yin, T. Liu, S. Chen, T. Liu and S. Cheng, *Applied Surface Science*, 2008, **255**, 2978-2984.
27. B. Yin, L. Fang, A. Q. Tang, Q. L. Huang, J. Hu, J. H. Mao, G. Bai and H. Bai, *Applied Surface Science*, 2011, **258**, 580-585.
28. W. A. Badawy, F. M. Al-Kharafi and A. S. El-Azab, *Corrosion Science*, 1999, **41**, 709-727.
29. L. Liu, J. Zhao, Y. Zhang, F. Zhao and Y. Zhang, *Journal of Colloid and Interface Science*, 2011, **358**, 277-283.
30. K. Tang, J. Yu, Y. Zhao, Y. Liu, X. Wang and R. Xu, *Journal of Materials Chemistry*, 2006, **16**, 1741-1745.
31. K. Tadanaga, K. Kitamuro, A. Matsuda and T. Minami, *Journal of Sol-Gel Science and Technology*, 2003, **26**, 705-708.
32. K. Tadanaga, N. Katata and T. Minami, *Journal of the American Ceramic Society*, 1997, **80**, 3213-3216.
33. B. Qian and Z. Shen, *Langmuir*, 2005, **21**, 9007-9009.
34. Y. Zhang, J. Wu, X. Yu and H. Wu, *Applied Surface Science*, 2011, **257**, 7928-7931.
35. Z. Guo, F. Zhou, J. Hao and W. Liu, *Journal of Colloid and Interface Science*, 2006, **303**, 298-305.
36. L. Feng, H. Zhang, P. Mao, Y. Wang and Y. Ge, *Applied Surface Science*, 2011, **257**, 3959-3963.
37. M. Fir, B. Orel, A. Šurca Vuk, A. Vilc□nik, R. Ješe and V. Francetic□, *Langmuir*, 2007, **23**, 5505-5514.
38. F. Zhang, L. Zhao, H. Chen, S. Xu, D. G. Evans and X. Duan, *Angewandte Chemie International Edition*, 2008, **47**, 2466-2469.
39. H. Chen, F. Zhang, S. Fu and X. Duan, *Advanced Materials*, 2006, **18**, 3089-3093.
40. Z. Wang, Y. Tian, H. Fan, J. Gong, S. Yang, J. Ma and J. Xu, *New Journal of Chemistry*, 2014, **38**, 1321-1327.
41. R. N. Wenzel, *Industrial & Engineering Chemistry*, 1936, **28**, 988-994.
42. A. B. D. Cassie and S. Baxter, *Transactions of the Faraday Society*, 1944, **40**, 546-551.
43. L. Liu, F. Xu, Z. Yu and P. Dong, *Applied Surface Science*, 2012, **258**, 8928-8933.
44. P. Wang, D. Zhang, R. Qiu and B. Hou, *Corrosion Science*, 2011, **53**, 2080-2086.

